# Fracture Density Estimation Using Spectral Analysis of Reservoir Reflections: A Numerical Modeling Approach

Fred Pearce, Daniel R. Burns, Rama Rao, Mark Willis, and Joongmoo Byun
Earth Resources Laboratory
Dept. of Earth, Atmospheric and Planetary Sciences
Massachusetts Institute of Technology
Cambridge, MA 02139
18 June 2003

**Abstract**

We use a 3-D finite difference numerical model to generate synthetic seismograms from a simple fractured reservoir containing evenly spaced, discrete, vertical fractures. The fractures are represented using a single column of anisotropic grid points. Analysis of seismic amplitudes and spectral characteristics were carried out on the top and base reservoir reflections as well as scattered wave coda for models with fracture spacing ranging from 0.01 to 0.1 fractures/m. Results show that the bulk scattered wave energy contained in a common shot gather increases greatly when the fracture spacing is greater than about 1/4 wavelength. Wavenumber spectra for integrated amplitude versus offset from a time window containing the base reservoir reflector show spectral peaks corresponding to the fracture spacing.

## 1. Introduction

Fractures are common within the subsurface and play a critical role in the mechanical and fluid flow properties of earth materials. In regions where the maximum compressive stress is vertical, open fractures will tend to be oriented vertically. The ability to interpret properties such as fracture spacing, orientation, and fluid content associated with such fracture systems is vital to the effective extraction and management of reservoir resources and the monitoring of contaminant migration. In particular, the ability to delineate zones of high fracture density is a key component in developing reservoir-scale fluid flow models.

The way in which fractures affect seismic waves depends on mechanical parameters, such as compliance and saturating fluid, and on their geometric properties, such as dimensions and spacing. If fractures are small relative to the wavelength of the seismic waves, the waves will be only weakly affected by the fractures. If fractures have characteristic lengths on the order of the wavelength then there will be scattering of energy due to the presence of the fractures. If fractures are spaced much closer than the wavelength of the seismic waves, then the medium will behave like a homogeneous, anisotropic equivalent medium. When fractures are spaced further away (about a quarter of a wavelength or more) the seismic waves will interact with the fractures and scatter appreciable energy from the wavefront.

Observations by previous researchers have demonstrated that scattering effects are sensitive to fracture density in real data as well as numerical and laboratory experiments (Ata and Michelena, 1995 and Rathore et al., 1994). In addition, numerical modeling of fractured media has proven to be an efficient way to explore the feasibility of using seismic waves to estimate fracture parameters. In particular, the applicability of finite difference methods to simulate wave propagation in a fractured elastic medium has been well documented in the literature (Shen and Toksoz, 2000, Daley et al. 2002, Nihei et al., 2002, Wu et al. 2002, Groenenboom and Falk, 1999, and Nakagawa et al. 2002).

Most previous work in estimating fracture parameters from seismic reflection data has focused on using an equivalent medium approach where the fractures themselves or the spacing between the fractures is assumed to be small relative to the wavelength of the seismic wave. In this paper, we explore the characteristics of reflected and scattered elastic waves that may be used to develop seismic attributes sensitive to fracture spacing. A 3D finite difference method is used to simulate wave propagation through a simple fractured reservoir which is modeled as a single horizontal layer containing parallel, evenly-spaced fractures. Previous work has shown that the finite difference method is accurate over a wide range of scattering regimes and can account for all converted waves and their interactions (Shen et al., 2002). Synthetic seismograms are generated along transects perpendicular and parallel to the fracture orientation and spectral characteristics of the wavefield scattered from the fracture zones are

analyzed. Our objective is to investigate how the intensity of seismic scattering changes with the spacing of discrete fractures, and develop potentially diagnostic seismic attributes sensitive to the fracture spacing. Our analysis focuses on the primary P-wave reflections from the top and bottom of the reservoir, as well as the scattered wave coda.

# 2. Background

The importance of fractures in the production and stimulation of reservoirs has resulted in considerable efforts to develop methods for fracture detection and characterization using seismic waves. In particular, offset dependent attributes are useful in characterizing vertical fractures because of the variation in incidence angle of waves impinging on the fractures. Much effort has focused on measuring amplitude variations with offset (AVO) for seismic reflections from a fractured reservoir (Gray et al., 2002, Perez et al., 1999, and Shen et al., 2002). Amplitude variation with offset and azimuth has been widely used to identify the orientation of vertical fractures with variable levels of success (Ruger, 1998; Mallick et al., 1998; Perez et al., 1999; Shen and Toksoz, 2000; Minsley et al., 2003). In these applications, the fractures are assumed to be small relative to the wavelength of the seismic waves. This allows the fractured medium to be modeled using an equivalent anisotropic medium (Schoenberg and Douma, 1988). Others have looked at shear wave data for fracture analysis (Lynn et al., 1995; Gaiser et al., 2002).

Shen et al. (2002) used numerical experiments and field data from a fractured reservoir in Venezuela to demonstrate the advantages of using attributes based on frequency variations with offset and azimuth (FVOA) in addition to AVOA based attributes to further constrain the interpretation of parameters related to the presence of vertically aligned fractures.

Recently, researchers have begun to focus on relaxing the assumption of relatively small fracture spacing by incorporating the effects of discrete fractures. Shen and Toksoz (2000) used stochastic models to generate heterogeneous fracture density distributions. They examined the effect of such fracture density variations using both time-domain and frequency-domain attributes and found that the presence of the fractures was more easily identified in the attributes associated with the base reflector. They concluded that first-order effects of fractures on FVO and AVO were controlled by the mean fracture density used in their stochastic fracture representation; however, they did not investigate systematic variations in fracture spacing. Daley et al. (2002) conducted 2D finite difference modeling of discrete fracture zones aimed at identifying scattering mechanisms and resolvability issues. They concluded that fracture tip diffractions and P-to-S conversions are the dominant scattered events from discrete fracture zones observable in surface seismic data, and identified fracture stiffness, spacing, and spatial scale as important parameters in controlling the resolvability of discrete fracture zones. Although their FD modeling and fracture representation are the same as what we use here, they do not specifically address the effect of fracture density on the development of the scattering wavefield.

Nakagawa et al. (2002) developed a hybrid numerical method that combines the plane wave method and the finite element method in order to examine the characteristics of the scattered wavefield from a layer containing discrete, vertical, evenly spaced fractures. However, their paper is more concerned with the presentation of the model and doesn't address variations in background velocities between fractured and unfractured layers, and doesn't vary the fracture spacing with the intention of developing seismic attributes sensitive to fracture spacing.

# 3. Modeling

As discussed in the previous section, a great deal of research has focused on the applicability of finite difference methods to modeling seismic scattering phenomena. In particular, Nihei et al. (2002) test the performance of the Coates and Schoenberg (1995) equivalent medium anisotropic cell approach for FD modeling of discrete fractures. The finite difference method is advantageous when modeling the scattering effect of discrete fractures because of its stability over a wide range of material property contrasts and its ability to model all wave types with minimal numerical dispersion and anisotropy. In addition, synthetic seismograms can be generated at any point within the model domain facilitating the simulation of surface seismic acquisition geometries.

We use the time domain, staggered grid finite difference code developed by Lawrence Berkeley National Laboratory (Nihei et al., 2002), which solves the 3-D, anisotropic stress-velocity formulation of the elastic wave equation (Levander, 1988). This formulation does not include intrinsic attenuation. The finite difference operator is $4^{th}$ order accurate in space and $2^{nd}$ order accurate in time.

Our numerical experiments use a simple reservoir geometry consisting of three horizontal layers. The first and third layer bound the reservoir and our homogeneous and isotropic with the same material properties. The second layer is 100-m thick and is where the fractures are placed. Figure 1 shows the model geometry for a fracture density of .02-frac/m and the background velocities used for each layer. Although absorbing boundary conditions are incorporated into the model, the boundaries are also placed far enough away so that any boundary reflections are not recorded in the seismograms during the time interval of interest.

The model uses a standard surface seismic reflection acquisition geometry, however, the source and receivers are embedded within the first layer to eliminate free surface effects. Receivers are placed in the crack normal and crack parallel directions with the first receiver fixed at the source. The receiver spacing is 20-m with the maximum source-receiver offset at 800-m which corresponds to a maximum angle of incidence of 45° relative to the top of the reservoir. A pressure source is used with a Ricker wavelet having a center frequency of 40-Hz. The model uses a uniform grid spacing of 5-m and a time step of .5-msec.

The fractures begin at a distance in the x-direction of 5-m from the edge of the grid and are then placed in even increments across the reservoir depending on the fracture spacing value. The source is also fixed at a point above the reservoir corresponding to a distance in the x-direction of 550-m from the edge of the model domain. As a result, the actual locations of fractures relative to receivers are different for models with different fracture densities.

In practice, we incorporate discrete vertical fracture zones into the reservoir layer using a single column of anisotropic grid points. The elastic properties of the discrete fractures are calculated using the Coates and Schoenberg (1995) thin anisotropic grid cell approach. The fractures are assumed to have negligible mass and thickness relative to the seismic wavelength in accordance with the linear slip model of Schoenberg (1980) for imperfect interfaces. The fractures are given equal normal and tangential stiffness of 8 x 10^8-Pa/m. We assume fracture zones are bed terminated and have constant fracture density across the reservoir for each of our simulations.

# 4. Model Results

We generated synthetic data using the finite difference code and model geometry presented in the previous section. Synthetic seismograms were produced for the no fracture case as well as for five different fracture density values: 0.01, 0.02, 0.0286, 0.04, and 0.1-frac/m. For the purposes of describing the model output, we will focus on two time windows of the time series. The first travel time window is bounded by the two coherent P-wave reflections and the second window contains all data after the P-wave reflection from the base of the reservoir.

## 4.1 Receiver Array Normal to Fractures

Figure 2 shows the vertical component of velocity recorded at each receiver position normal to the fractures for each fracture density case. The no fracture case is useful for identifying the main P- and S-wave reflections from the top and bottom of the reservoir. The first time window contains only the coherent P-wave reflections. However, careful observation shows a third event separates from the 2$^{nd}$ P-wave reflection at large offsets. The event is associated with the downgoing P-wave reflected as an S-wave at the base of the reservoir, and then converted back to a P-wave upon leaving the reservoir. Because of this conversion, the event has a slightly slower move-out velocity than the primary P-wave reflection from the base of the reservoir.

The dominant events in the second time window are the S-wave reflections, which show rapid increases in amplitude as offset increases because we are looking at only vertical particle velocities from our receivers. The S-wave reflection from the top of the reservoir has a relatively large amplitude while the S-wave from the base of the reservoir has a much smaller amplitude at least partially due to the additional conversions to P-waves as seen in the first time domain.

As we begin to incorporate fractures into the reservoir, we see a drastic change in the character of the time series. For the .01-fractures/meter case, the first time window shows the P-wave reflection from the top of the reservoir remains relatively unaffected while the P-wave reflection from the base of the reservoir shows significant interference from scattered events starting at about 400-m offset. The curvature of the second P-wave reflection increases owing to a reduced effective velocity in the reservoir due to the presence of the fractures.

In the second time window, we see that both S-wave reflections have become difficult to follow. The S-wave reflection from the top of the reservoir is affected by interference from scattered waves and shows better coherence at larger offsets where its amplitude is large. However, the S-wave reflection from the base of the reservoir is completely drowned out by scattered events due to the presence of the fractures. Overall, the second

time window is dominated by many different events derived from interactions with the fractures. Close observation shows these events seem to focus at offsets between 200-m and 600-m and at travel times after the S-wave reflection from the top of the reservoir.

As we increase the fracture density to .02-fractures/meter, the same trends are observed. In the first time window, the P-wave reflection from the top of the reservoir shows an appreciable decrease in amplitude with offset. The P-wave reflection from the base of the reservoir becomes more incoherent at smaller offsets and is more difficult to follow from receiver to receiver. The decrease in amplitude of both P-wave reflections can be attributed to a decrease in the impedance contrast between the two layers and to interference from scattered waves with shorter travel paths.

In the second time window, the S-wave reflection from the top of the reservoir is only observable at very large offsets and the S-wave reflection from the base of the reservoir is absent. The scattered events have a very similar appearance to those for the .01-fractures/meter case except there doesn't seem to be a focus of scattered energy in the mid-offset receivers.

For the .0283-fractures/meter case, the first time window shows the P-wave reflection from the top of the reservoir is being interfered with at much smaller offsets (~400-m). In addition, we observe a large increase in the amplitude of events at large offsets within the first time window. These observations suggest shorter travel paths and larger amplitudes for these scattered events.

The second time window contains a relatively large amplitude S-wave reflection from the top of the reservoir whose amplitude reaches a maximum between 400-m and 500-m offsets. In fact, scattered events tend to have large amplitudes and arrive at earlier times than the previous cases. Again, these observations support shorter travel paths and larger amplitudes for scattered events.

The .04-fractures/meter case shows a sudden change in the character of the time series. In the first time window, the P-wave reflection from the top of the reservoir is still interfered with at larger offsets but the magnitude of the interference is smaller. The P-wave reflection from the base of the reservoir becomes much more coherent; however, it is now interfered with by an event that arrives at almost the same time even at zero offset and has a very similar move-out behavior. In general, we can now clearly observe that the apparent velocity of the P-wave reflection from the base of the reservoir has decreased substantially from the case with no fractures.

For the second time window, we see that the S-wave reflection from the top of the reservoir is clear and its amplitude increases with offset. The amplitude of the scattered events has decreased substantially and there are patches within the time series where no noticeable scattered energy is present. However, the weak scattered events that remain still show the linear move-out trend observed in the previous fracture density cases.

The .1-fractures/meter case, we see the almost the same behavior as the no fracture case. In the first time window, we only observe the P-wave reflections from the top and bottom of the reservoir. The amplitude of the P-wave from the top of the reservoir decreases more rapidly with offset than the no fracture case. The move-out velocity of the P-wave reflection from the bottom of the reservoir is much smaller. In the second time window, the S-wave reflection from the top of the reservoir is larger in amplitude. Almost no scattered energy is present within either time window. These observations are consistent with the equivalent medium representation that is applicable when fracture spacing is much smaller than the wavelength of the seismic waves.

## 4.2 Receiver Array Parallel to Fractures

The vertical component of velocity for receivers parallel to the fractures can be observed for each fracture density case in Figure 3. As we expect, the no fracture case has identical time series data as obtained from receivers in the normal direction. For the .01-fractures/meter case, we observe very little change in the first time window. Both P-wave reflections are coherent and the apparent velocity of the P-wave reflection from the base of the reservoir is slightly slower than the no fracture case.

For the second time window, the S-wave reflection from the top of the reservoir is observable at only large offsets. The scattered events are much more coherent from receiver to receiver and seem to have move-out trends similar to the P-wave reflections. In addition, the scattered events have smaller amplitudes than those obtained from the receivers normal to the fractures.

The .02-fracture/meter case shows similar trends to the .01-fractures-meter case. The P-wave reflection from the top of the reservoir is coherent across all offsets. However, the P-wave reflection from the base of the reservoir is difficult to follow at large offsets and has significant interference from scattered events at small offsets. The S-wave reflection from the top of the reservoir can only be observed at large offsets. Again, we see that the scattered events have move-out trends similar to the P-wave reflections.

For the .0283-fractures/meter case, we again see that the P-wave reflection from the top of the reservoir is unaffected. However, the P-wave reflection from the base of the reservoir is loses coherence at an offset of about 400-m offset. The S-wave reflections can not be distinguished; however, there is a focusing of large amplitude scattered energy in around the time interval of the S-wave reflections. In general this scattered energy has a similar move-out trend but is more concentrated particularly at small offsets.

In the .04-fractures/meter case, both P-wave reflections are very coherent and there is little scattered energy present. In general the .04-fractures/meter case is similar to the .1-fractures/meter case with a couple of exceptions. The .04-fractures/meter case has some small interference of the P-wave reflection from the base of the reservoir as compared to the .1-fractures/meter case. Also, the .04-fractures/meter case has enough residual scattered energy to blur the S-wave reflection from the base of the reservoir while this event is clear in the .1-fractures/meter case.

### 4.3 Snapshots

Snapshots of the wavefield in the presence of discrete fracture zones highlight the different scattering events and their interactions. Figure 4 shows the vertical component of velocity after .3-seconds for a fracture density of .02-fractures/meter. We see that the P-wave reflection from the top of the reservoir remains relatively coherent, while the P-wave reflection from the base of the reservoir is much more effected by the discrete fractures. This figure also illustrates the difference in coherence of the scattered wavefield normal and parallel to the fractures. Normal to the fractures (Figure 4a), interference of scattered waves from the fractures results in a complex wavefield. Fractures act as secondary sources and multiple scattering effects can be seen. Parallel to the fractures the wavefield is much more coherent. The fractures appear to act more as a waveguide.

## 5. Analysis

The purpose of this section is to present methods developed to quantify the effect of variations in fracture density in our models.

### 5.1 Velocity Anisotropy

In general, aligned fractures will result in velocity anisotropy, which is often used as a measure of fracture intensity. Therefore, we examined the effect of variable fracture density on the normal move-out (NMO) velocity estimated by following the P-wave reflections as a function of offset (note: although our models are generated for a single source position with multiple receivers, and therefore are common shot gathers, we treat them as if they were a CMP gather). In our simple model, the normal move-out (NMO) velocity of the upper layer will simply be the P-wave velocity specified for the upper layer, 3000-m/s. However, energy reflecting from the base of the reservoir will pass through both layers and potentially fractures as well. Therefore, the NMO velocity of the P-wave reflection from the base of the reservoir should depend on the fracture density and this effect should be strongest when measured normal to the fractures.

To estimate the NMO velocity, we pick the closest peak in amplitude associated with the P-wave reflection from the base of the reservoir at every offset and use the hyperbolic move-out equation to fit the time values of these peaks using a linear least squares regression. Figure 5a shows the best-fit velocity curve for the .02-fractures/meter case and shows appreciable variation in the peak amplitudes about the best-fit model.

Using this approach, we calculated NMO velocities parallel and perpendicular to the fractures for each fracture density case (Figure 5b). In the parallel direction, the NMO velocities remain relatively constant although slight variations exist at fracture density values between .01-fractures/meter and .0283-fractures/meter. Conversely, the NMO velocities in the normal direction decrease as the fracture density increases and again we see irregular fluctuations in NMO velocity for the fracture density values between .01-fractures/meter and .0283-fractures/meter.

As we pointed out in the previous section, the presence of discrete fractures in our model affects the coherence of the P-wave reflections because of interference from scattered events. Therefore, as our observations indicate, we expect to see the greatest variability in NMO velocity for fracture density values associated with the greatest amount of scattering. This is important because using velocity anisotropy alone to estimate the fracture density associated with large discrete fractures may lead to erroneous results.

## 5.2 Bulk Scattering

In addition to velocity anisotropy, it is also important to quantify the amount of scattering present in the different fracture density cases. To calculate the amount of scattered energy in each time series output, we select a time window that incorporates as much of the data as possible (Figure 5c). We then take the absolute value of the windowed amplitudes and sum them to get a single integrated amplitude value. This procedure is done for the normal and parallel directions and for each fracture density value.

Figure 5d shows the resulting integrated amplitude values as a function of fracture density and orientation. The shapes of the integrated amplitude curves are nearly identical in the normal and parallel case. However, the normal case has much larger integrated amplitude values in the fracture density range between .01-fractures/meter and .0283-fractures/meter. The integrated amplitude values rise sharply as you move away from the no fracture case, reach a peak at the .0283-fractures/meter case, and decline more gradually towards the .1-fractures/meter case. The fracture density of .0283-fractures/meter obtains a value almost three times that of the case with no fractures in the normal direction. The .1-fractures/meter case falls to the no fracture case in the normal direction and actually falls below the no fracture case in the parallel direction, due to a change in AVO response.

## 5.3 Spectral Analysis of Integrated Amplitude vs. Offset

We have demonstrated that the strongest scattering of seismic energy occurs for the fracture cases between .01-fractures/meter and .0283-fractures/meter. Now we will extend the integrated amplitude approach to develop an offset dependent attribute sensitive to fracture spacing within this strong scattering regime. We will focus on the P-wave reflection from the base of the reservoir and construct a robust window to capture this event and scattered events with similar arrival times. As we have shown, the P-wave reflection from the base of the reservoir is difficult to follow because of interference from scattered events. For this reason, we use a relatively large window based upon the NMO velocity of the P-wave reflection from the top of the reservoir. However, the P-wave reflection from the top of the reservoir does not sample the fractures directly and so will be excluded from the window. The same window is used for all fracture density cases making it robust in its application. Amplitude values within the window are rectified and then summed to give a single integrated amplitude value for each offset.

Figure 6 shows the plots of integrated amplitude vs. offset for each of the fracture density values with receivers normal to the fractures. In the absence of strong scattering, as in the no fracture case, we see that the curves show a smooth line dominated by the AVO response of the P-wave reflection from the base of the reservoir along with secondary effects from P to S conversions as described in the Data section. For the fracture density range associated with strong scattering, we also observe an AVO trend in the integrated amplitudes with offset; however, there are also periodic fluctuations about the AVO trend. These fluctuations are the greatest for the .01-fractures/meter and .02-fractures/meter case and are substantially less in the .0283-fractures/meter case.

Figure 7 displays the same integrated amplitude vs. offset plots parallel to the fractures. We see the same trends in these plots but they lack the oscillations about the AVO trend. The difference between the normal and parallel cases is consistent with our earlier observation that scattered events in the parallel case tend to have move-out trends similar to the primary reflections. Therefore, we conclude that the interference patterns observed in the integrated amplitude vs. offset from the normal direction may have a direct correlation with fracture density.

To test this hypothesis, we transform the integrated amplitude vs. offset data in Figure 6 to the amplitude vs. wavenumber domain using the Fast Fourier Transform (FFT). Since the resulting spectra are dominated by the AVO trend in the data, we remove this dominant trend by normalize the spectra. If the method is to be robust, the fracture density estimate must be insensitive to the spectra used to normalize. To address this issue, we normalize the spectrum obtained from each of the strong scattering fracture density values (i.e. .01- .02-, and .0286-fractures/meter) with each of the spectra obtained from the weak scattering regime (Figure 8). Several important observations can be made from the resulting normalized spectra:

1) Peaks in the normalized spectra correspond to the input fracture density values for the .01-fractures/meter and .02-fractures/meter cases.
2) The ability to resolve the .0283-fractures/meter spacing is beyond the resolution of the analysis, which is determined by the receiver spacing.
3) The method is robust with respect to the spectrum used to remove the dominant trend and gives accurate estimates even when the .04-fracture/meter spectrum is used.

## 6. Discussion and Conclusions

We used a finite difference code to model scattering effects from discrete, vertical fractures with variable fracture spacing. Observations from vertical velocity time series show that scattering along receiver transects normal to fractures contain more complex wave patterns while receiver transects parallel to fractures tend to only have hyperbolic move-outs similar to the primary P-wave reflections. This implies that stacking data obtained normal to fractures may remove valuable information regarding fracture parameters if those fractures behave as scatterers.

Analysis of NMO velocities associated with the P-wave reflection from the base of the reservoir showed that using velocity anisotropy to estimate fracture intensity might lead to erroneous results when fractures strongly scatter seismic waves. For our numerical experiment, this strong scattering regime occurs between fracture densities of .01-fractures/meter and .0283 fractures/meter. Given the background velocities in our reservoir, this strong scattering regime corresponds to spacing between the fractures of about a P-wavelength to about half an S-wavelength. This observation agrees with well-established theory on scattering of waves by heterogeneities.

We use a robust window about the P-wave reflection from the base of the reservoir to calculate integrated amplitude values as a function of offset. When receivers are normal to the fractures, we observe periodic fluctuations about the general AVO trend within the strong scattering regime. Transforming this information to the wavenumber domain yield peaks in the spectra that correspond to the fracture density of the model, which can be easily, observed when the general trend is removed. The peaks in the spectra are not sensitive to the model used to remove the general trend.

However, two important issues in using this method were identified when attempting to resolve the fracture density of .0283-fractures/meter. The spatial resolution of this method is controlled by the spacing of the receivers. For a specified maximum fracture density to be resolved, the receiver spacing must be at least half of that maximum fracture density as governed by the Nyquist criterion.

Another consideration is that the amplitudes of the fluctuations in the .0283-fractures/meter case are much smaller than in the other two cases that were successful. This may be due to the window of the data not capturing enough of the scattered energy responsible for the interference patterns that lead to the fracture density estimation. In fact, this observation can be somewhat validated by examining the time series for the .0283-fractures/meter case, which show a lack of almost any events within the time window used for this analysis. Instead, this case shows strong scattered energy just below the window used in this analysis. Therefore, the optimal window used for this method may depend on the fracture density and may require additional constraints.

We have focused our more detailed spectral analysis on the time window around the P-wave reflection from the base of the reservoir. However, we have shown that a great deal of energy is scattered into events that arrive significantly later than the primary P-wave reflections. As we have stated, the time series data normal to the fractures have many different scattered events with different apparent NMO velocities while the time series parallel to the fractures have move-out trends that follow the primary reflections. Therefore, examining scattering derived coda using the two-dimensional FFT may show some relationship between apparent velocity and peak amplitude wavenumber or frequency that relate to fracture spacing. In addition, time shifting the windowed data used in the two-dimensional FFT using an NMO velocity can separate the spectra of individual events with different move-out trends. An example of two-dimensional FFT output for the scattered wave coda from the four fracture cases with the strongest scattering are shown in Figure 9.

In this paper we have only investigated the effect of variations in the spacing between discrete fractures. The effect of fracture stiffness, fracture zone thickness (in this study the fracture zones were set to the grid size of 5 meters), heterogeneous fracture spacing, and reservoir thickness on the scattered wavefield should also be investigated. In addition, we have only focused on one component of the wavefield. It would be beneficial to look at horizontal components as well in order to investigate the relative strength of P and S wave scattering.

## 7. Acknowledgements

This work was supported by the Department of Energy grant number DE-FC26-02NT15346, ENI S.p.A. AGIP, and the Earth Resources Laboratory Founding Member Consortium.

# References


Ata, E., and Michelena, R. J., 1995, Mapping distribution of fractures in a reservoir with P-S converted waves, The Leading Edge, v. 12, p. 664-676.

Coates, R. T., and Schoenberg, M., 1995, Finite-difference modeling of faults and fractures, Geophysics, **60**, n5, 1995.

Daley, T.M., et al., 2002, Numerical modeling of scattering from discrete fracture zones in a San Juan Basin gas reservoir, 72nd Ann. Int. Mtg. Soc. Expl. Geophys. Expanded Abstracts.

Gaiser, J.E., Loinger, E., Lynn, H., and Vetri, L., 2002, Birefringence analysis at Emilio Field for fracture characterization, First Break, v. 20.8, p.505-514.

Gray, D., Roberts, G., and Head, K., 2002, Recent advances in determination of fracture strike and crack density from P-wave seismic data, The Leading Edge, v. 22, p. 280-285.

Groenenboom, J., and Falk, J., 2000, Scattering by hydraulic fractures: Finite-difference modeling and laboratory data, v. 65, p. 612-622.

Lynn, H. B., Simon, K. M., Layman, M., Schneider, R., Bates, C. R., and Jones, M., 1995, Use of anisotropy in P-wave and Swave data for fracture characterization in a naturally fractured gas reservoir: The Leading Edge, **14**, 887-893.

Mallick, S., Craft, K.L., Meister, L.J., and Chambers, R.E., 1998, Determination of the principal directions of azimuthal anisotropy from p-wave seismic data. Geophysics, v. 63, p. 692-706.

Minsley, B.J., Burns, D.R., and Willis, M.E., 2003, Fractured reservoir characterization using azimuthal AVO, ERL Industrial Consortium Annual Report, MIT.

Nakagawa, S., Nihei, K.T., and Myer, L.R., 2002, Numerical simulation of 3D elastic wave scattering off a layer containing parallel periodic fractures, 72nd Ann. Int. Mtg. Soc. Expl. Geophys. Expanded Abstracts.

Nihei, K.T., et al., 2002, Finite difference modeling of seismic wave interactions with discrete, finite length fractures, 72nd Ann. Int. Mtg. Soc. Expl. Geophys. Expanded Abstracts.

Perez, M.A., Grechka, V., and Michelena, J., 1999, Fracture detection in a carbonate reservoir using a variety of seismic methods, Geophysics, v. 64, p. 1266-1276.

Rüger, A., 1998, Variation of P-wave reflectivity with offset and azimuth in anisotropic media: Geophysics, 54, 680-688.

Schoenberg, M., Sayers, C.M., 1995, Seismic anisotropy of fractured rock, Geophysics, v. 60, p. 204-211.

Shen, F., Sierra, J., Burns, D.R., and ToksÖz, M.N., 2002, Case History: Azimuthal offset-dependent attributes applied to fracture detection in a carbonate reservoir, Geophysics, v. 67, p. 355-364.

Shen, F. and ToksÖz, M.N., 2000, Scattering characteristics in heterogeneously fractured reservoirs from waveform estimation, Geophys. J. Int., v. 140, p. 251-266.

Wu, C., Harris, J.M., and Nihei, K.T., 2002, 2-D finite-difference seismic modeling of an open fluid-filled fracture: comparison of thin-layer and linear-slip models, 72nd Ann. Int. Mtg. Soc. Expl. Geophys. Expanded Abstracts.

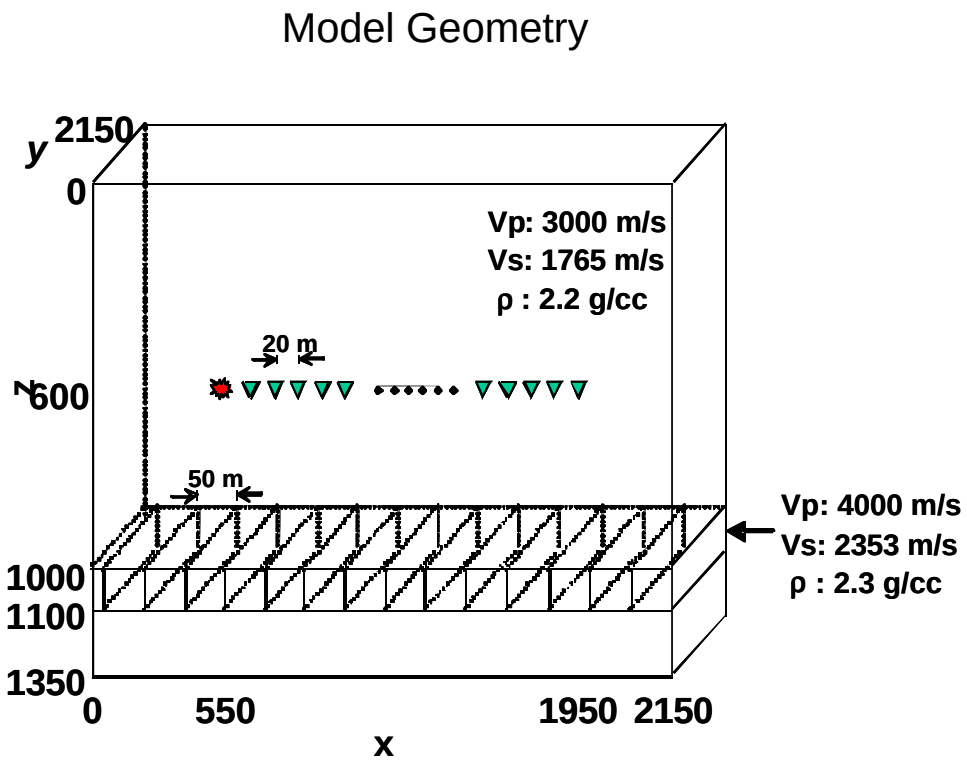


Figure 1 – The model geometry for the .02-fractures/meter case showing the source and receiver locations, fracture locations, and velocity and density parameters

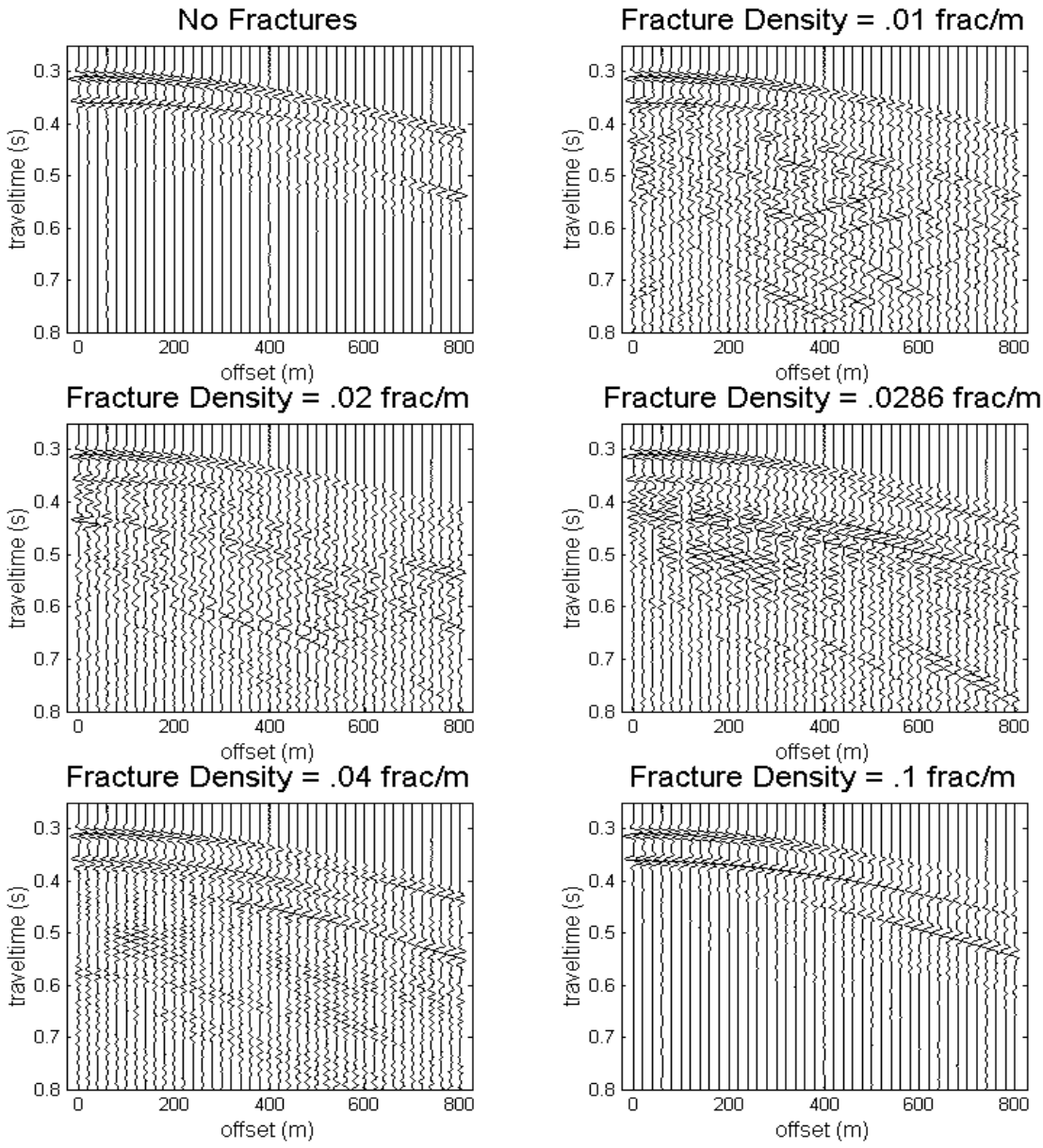


Figure 2 – Vertical component of velocity normal to fractures for each fracture density case

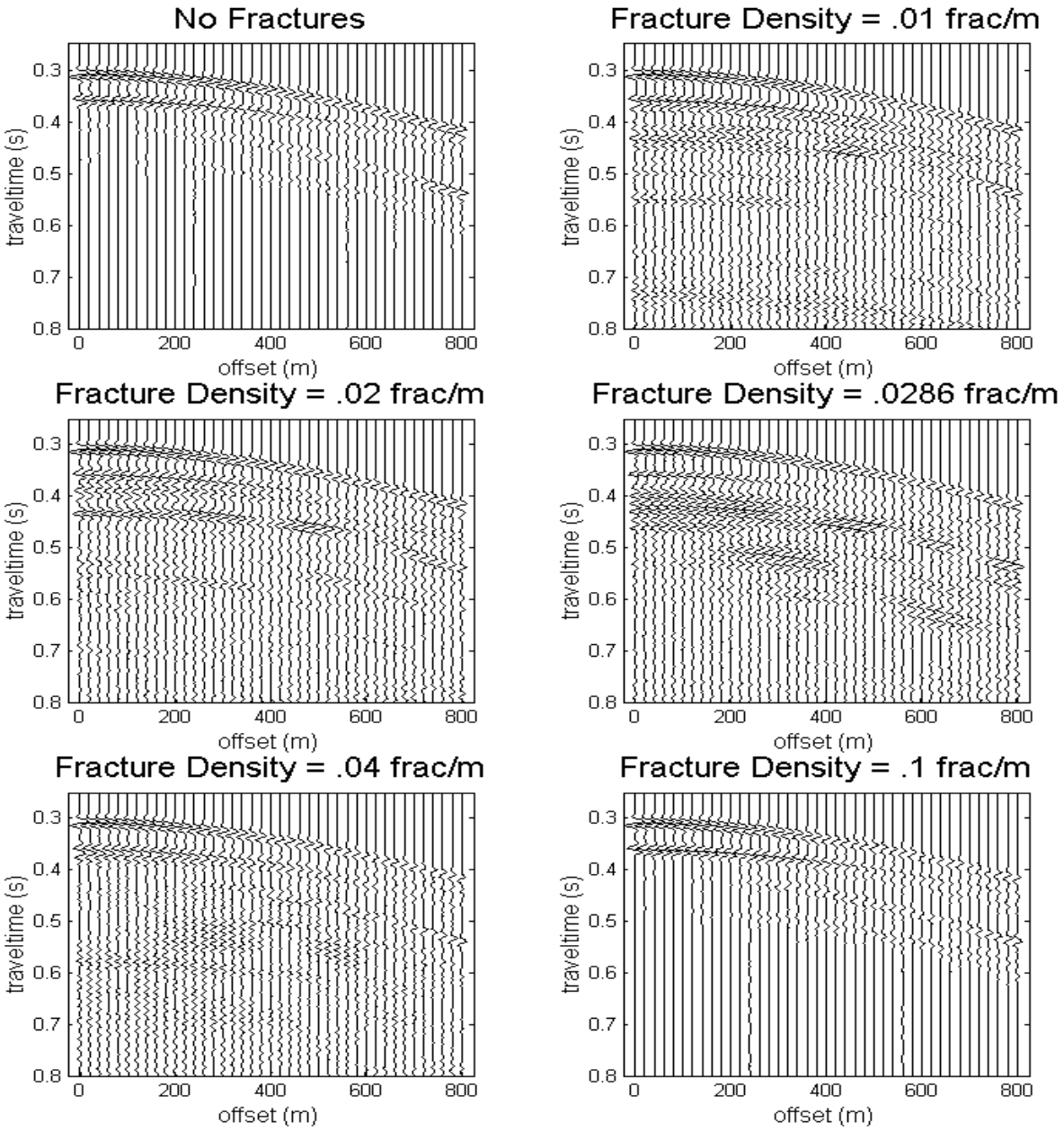


Figure 3 – Vertical component of velocity parallel to fractures for each fracture density case

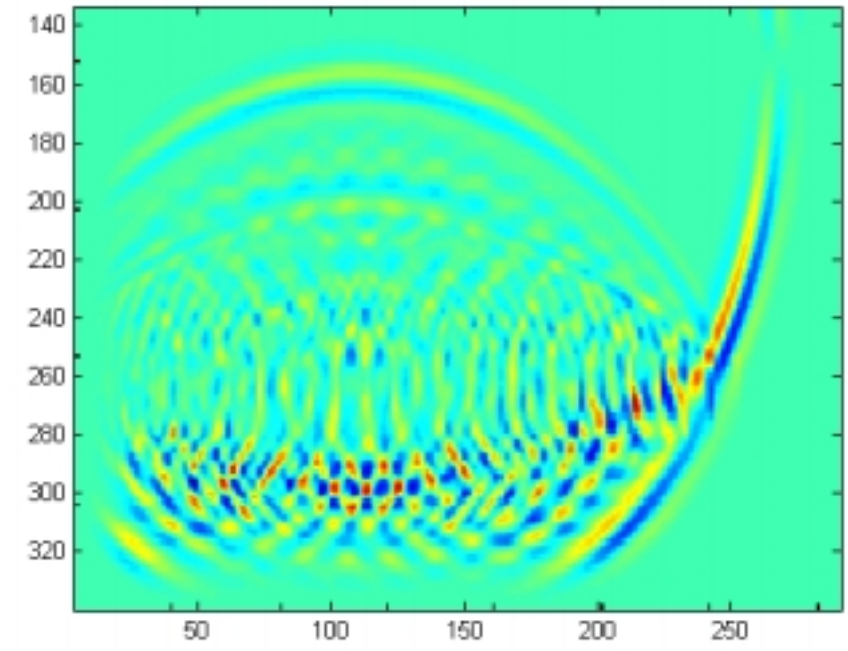


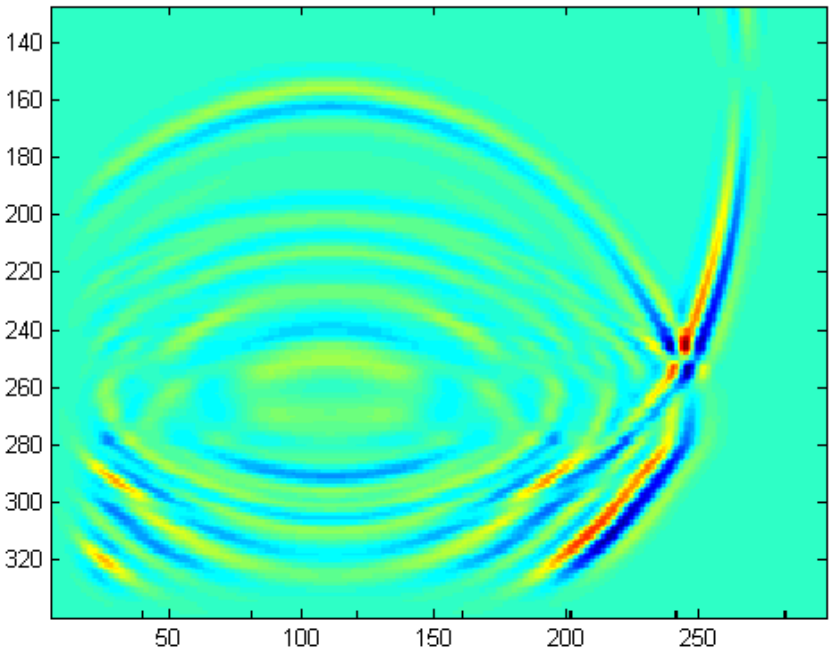


Figure 4 – Snapshots of the vertical component of velocity in the normal (a) and parallel directions (b) at a time of .3-seconds

a)

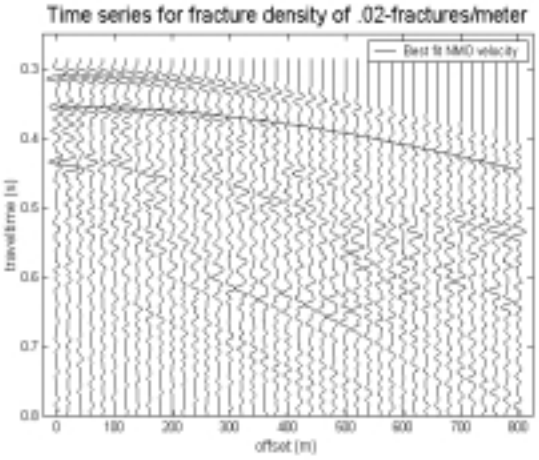


b)

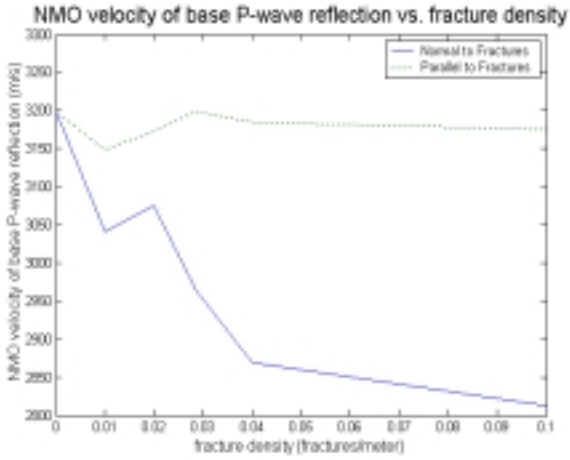


c)

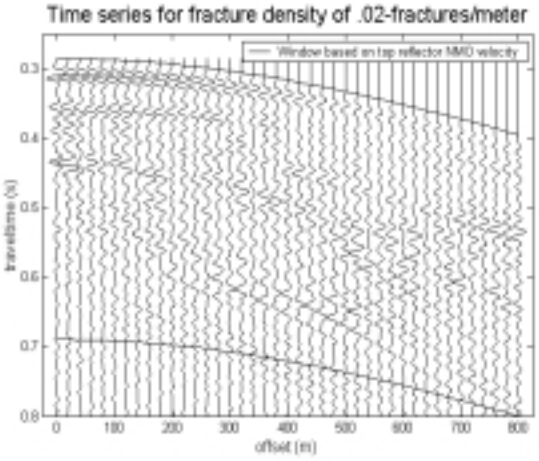


d)

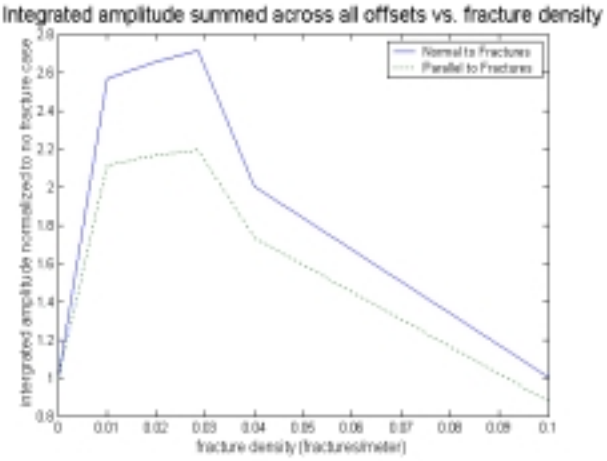


Figure 5 – a) shows the traces for the .02-fractures/meter case where the bold line represents the best fit NMO velocity, b) plot with the best fit NMO velocity for each fracture density in the normal and parallel directions, c) shows the windowing used to calculate integrated amplitudes summed across all offsets in d) for the normal and parallel case

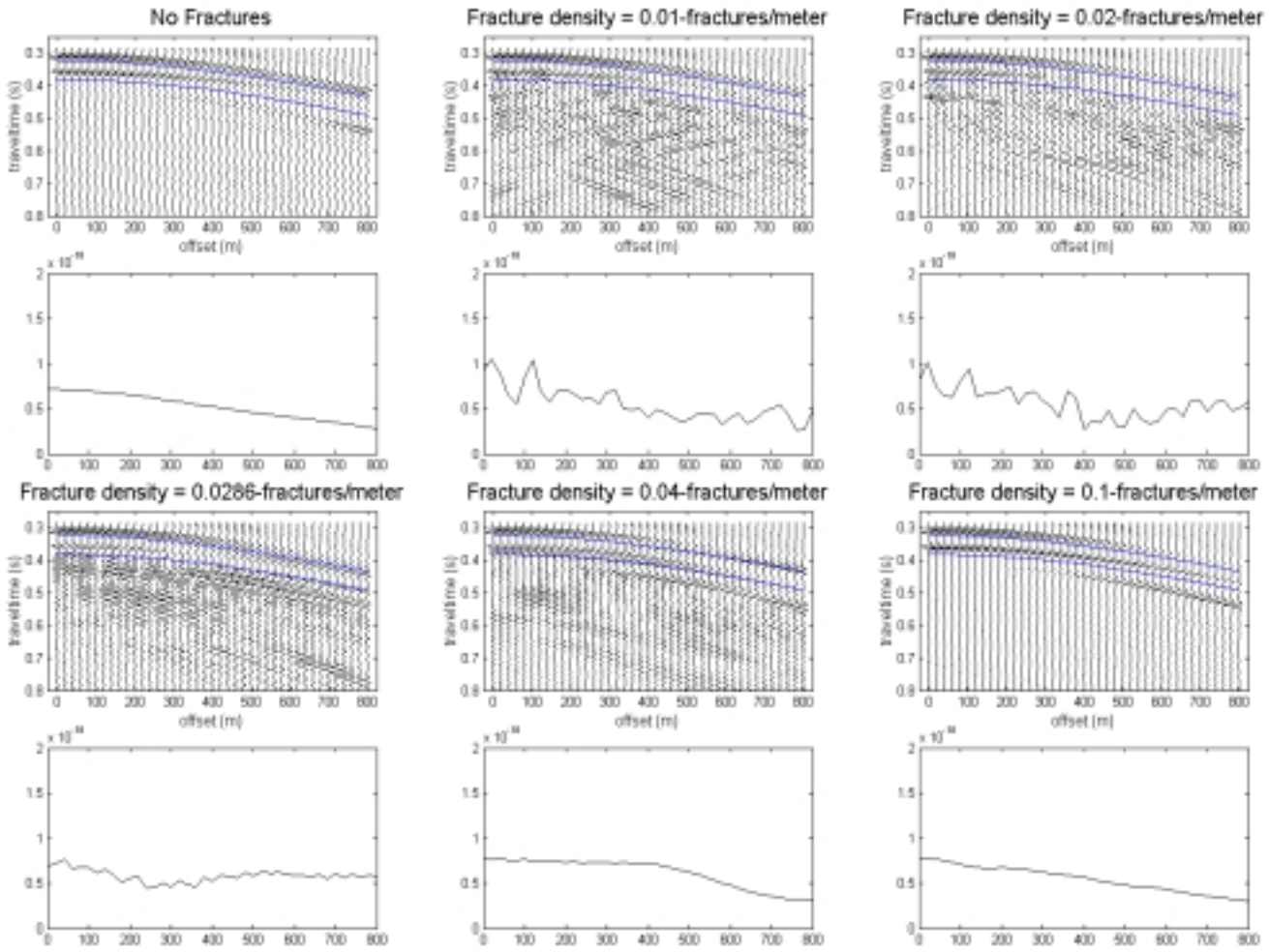


Figure 6 – Integrated amplitude as a function of offset for receivers normal to fractures. Blue lines show window used in calculations.

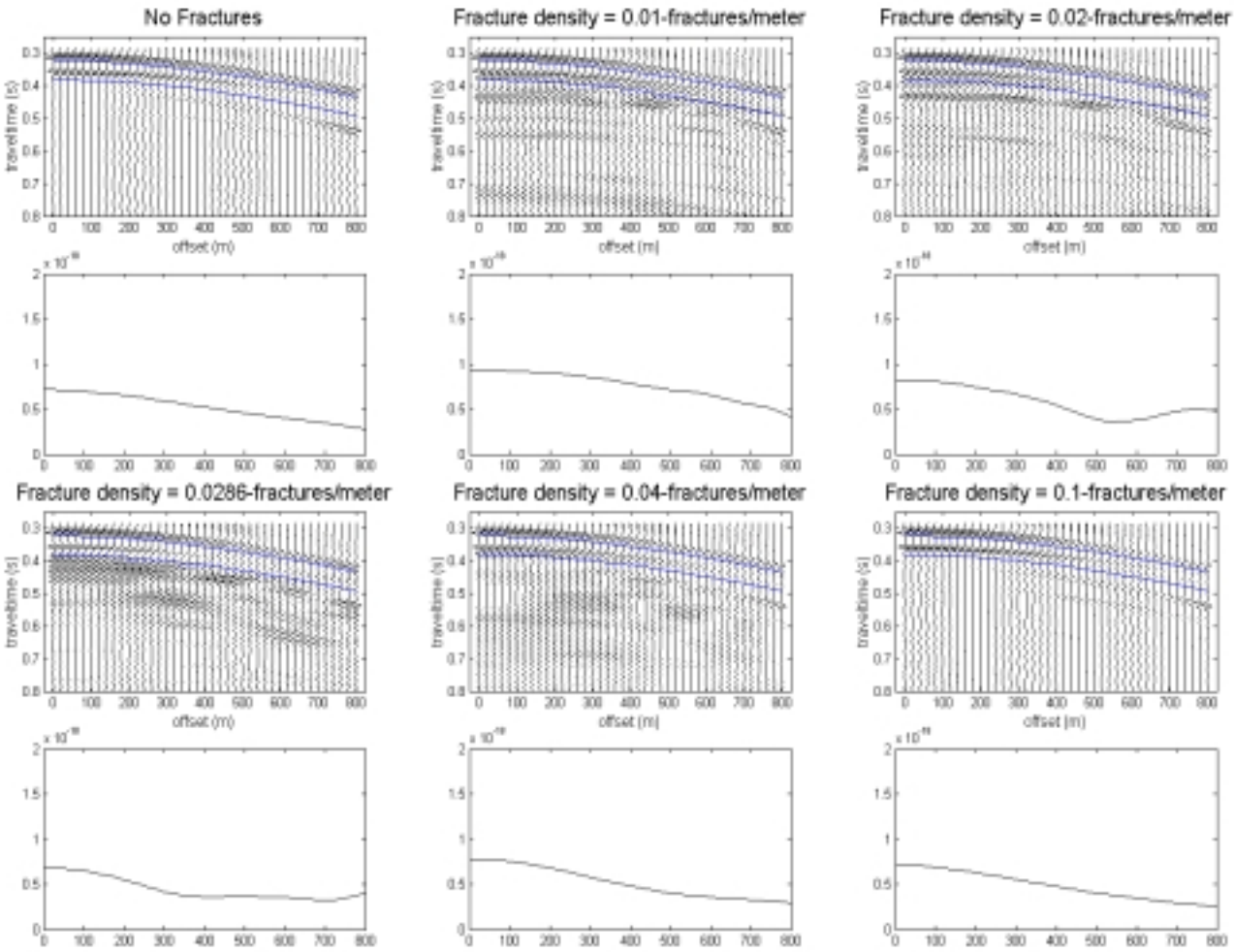


Figure 7 – Integrated amplitude as a function of offset for receivers parallel to fractures. Blue lines show window used in calculations.

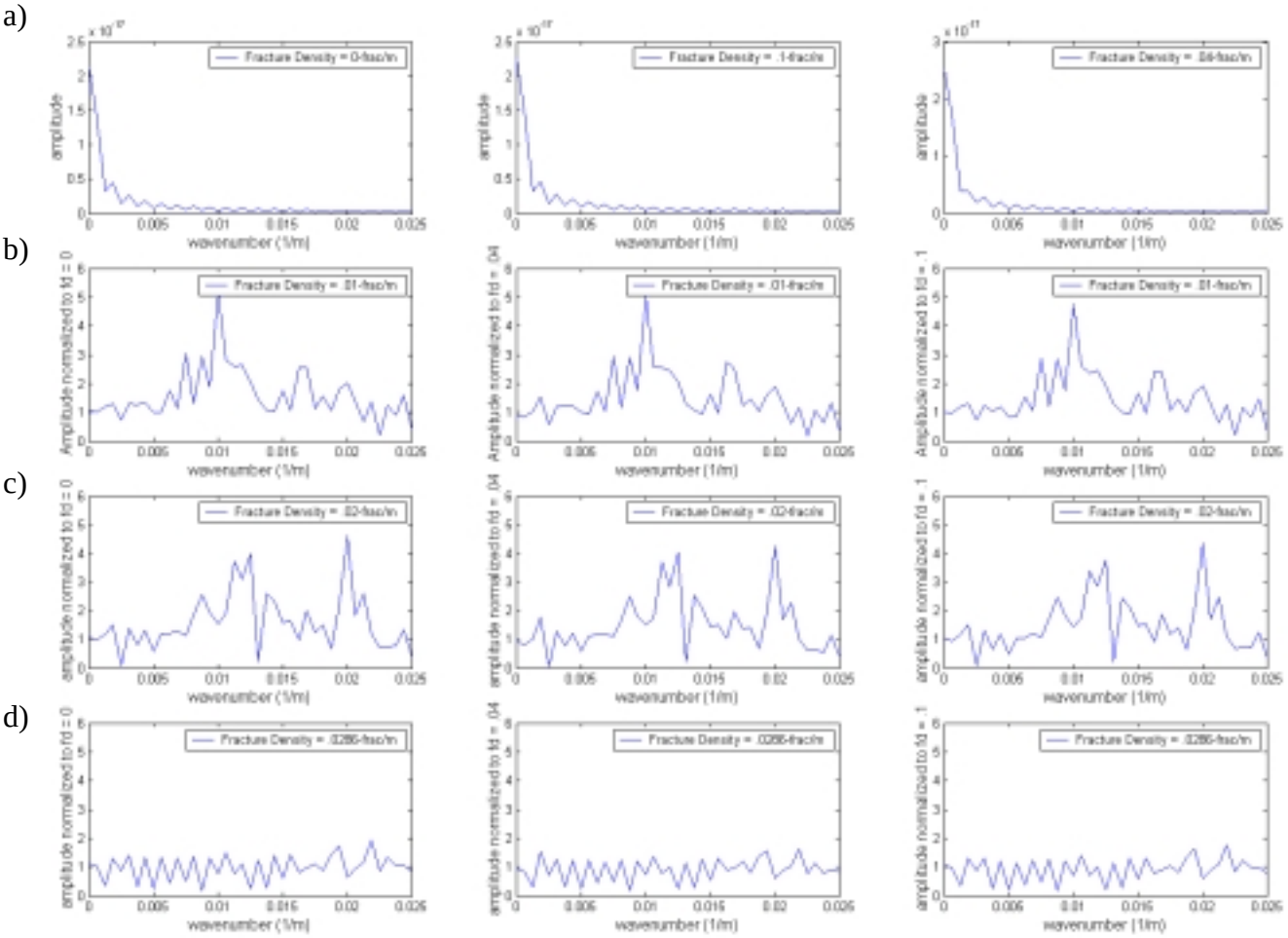


Figure 8 – Spectra of integrated amplitude vs. offset curves in Figure 6. a) Spectra used for normalizing (from left to right) - no fracture spectrum, .1-fractures/meter spectrum, and .04-fractures/meter spectrum. b) Normalized spectra for the .01-fractures/meter case, c) Normalized spectra for the .02-fractures/meter case, and d) Normalized spectra for the .0283-fractures/meter case

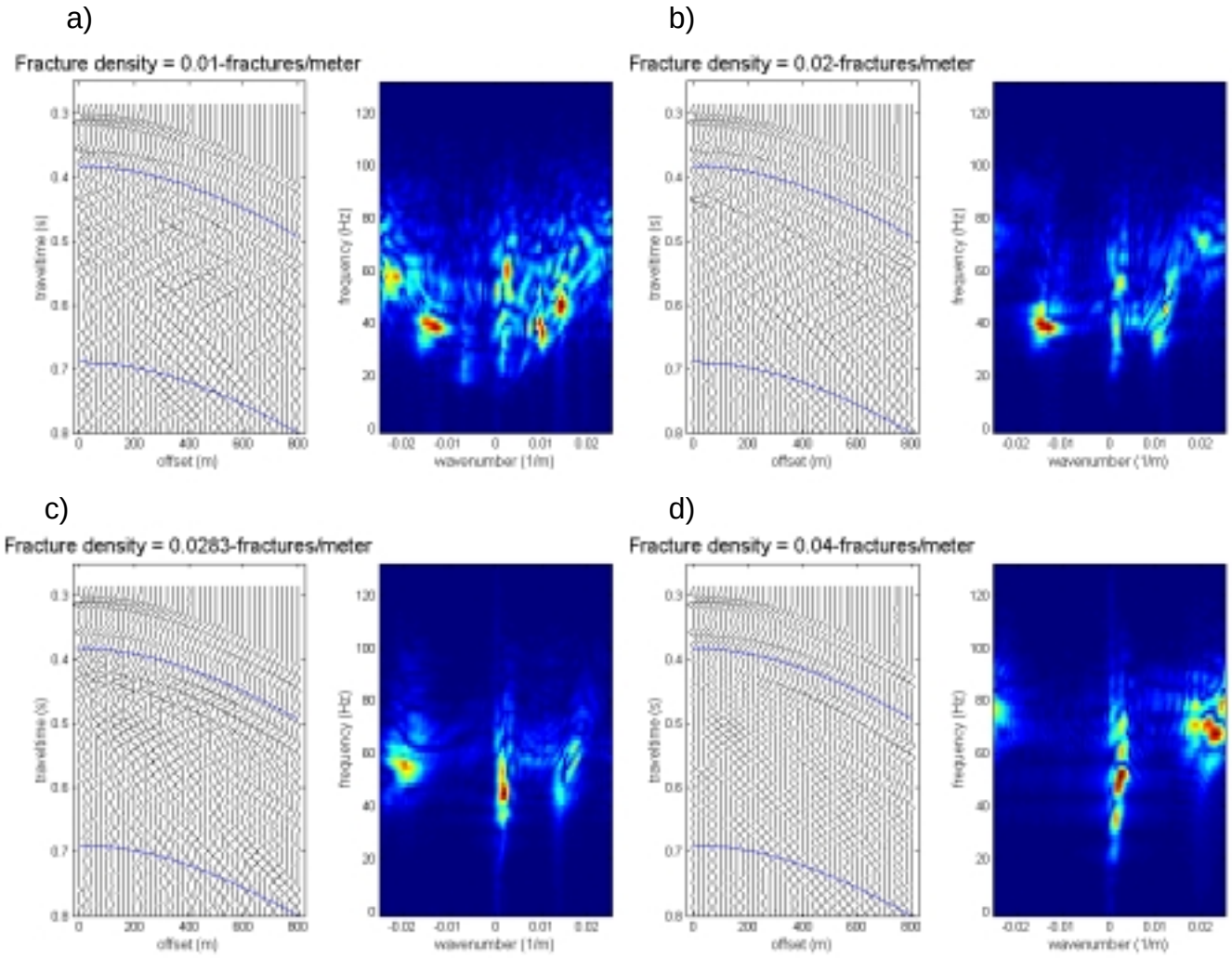


Figure 9 – Two-dimensional FFT output generated using NMO corrected time series data from the window enclosed by blue lines for a) fracture density of .01-fractures/meter, b) fracture density of .02-fractures/meter, c) fracture density of .0283-fractures/meter, and d) fracture density of .04-fractures/meter.